Tenth U.S. National Conference on Earthquake Engineering
Frontiers of Earthquake Engineering
July 21-25, 2014
Anchorage, Alaska

CYCLIC MOBILITY AND POST-LIQUEFACTION BEHAVIORS OF GRANULAR SOILS UNDER CYCLIC LOADING: MICROMECHANICAL PERSPECTIVES

J. Wei[1] and G. Wang[2]

ABSTRACT

Cyclic mobility occurs in a broader range of granular soils. It is characterized by progressive accumulation of shear deformations and progressive reduction in the effective pressure under cyclic loading, resulting in the triggering of liquefaction and large permanent displacements in the post-liquefaction stage. In this study, the micromechanical characteristics of the granular soils are investigated using the Discrete Element Method. It is observed that the cyclic mobility and post-liquefaction behaviors are closely related to the micromechanical structure, indicated by evolution of the coordination number, local strain measures, and non-affine displacements. A new index, termed as centroid distance, is proposed to quantify the change of the microscopic configuration of the granular packing. The index is found to have a strong correlation to the cyclic mobility of the granular packing in the post-liquefaction stage. The study provides significant insights into the fundamental mechanisms of cyclic mobility and liquefaction in granular soils from micromechanical perspectives.

[1] Graduate Student Researcher, Dept. of Civil and Environmental Engineering, The Hong Kong University of Science and Technology, Hong Kong
[2]Assistant Professor, Dept. of Civil and Environment al Engineering, The Hong Kong University of Science and Technology, Hong Kong. Corresponding Author. Email: gwang@ust.hk

Wei J., Wang G. Cyclic mobility and post-liquefaction behaviors of granular soils under cyclic loading: micromechanical perspectives. *Proceedings of the 10th National Conference in Earthquake Engineering*, Earthquake Engineering Research Institute, Anchorage, AK, 2014.

Tenth U.S. National Conference on Earthquake Engineering
Frontiers of Earthquake Engineering
July 21-25, 2014
Anchorage, Alaska

Cyclic Mobility and Post-liquefaction Behaviors of Granular Soils under Cyclic Loading: Micromechanical Perspectives

J. Wei[1] and G. Wang[2]

ABSTRACT

Cyclic mobility occurs in a broader range of granular soils. It is characterized by progressive accumulation of shear deformations and progressive reduction in the effective pressure under cyclic loading, resulting in the triggering of liquefaction and large permanent displacements in the post-liquefaction stage. In this study, the micromechanical characteristics of the granular soils are investigated using the Discrete Element Method. It is observed that the cyclic mobility and post-liquefaction behaviors are closely related to the micromechanical structure, indicated by evolution of the coordination number, local strain measures, and non-affine displacements. A new index, termed as centroid distance, is proposed to quantify the change of the microscopic configuration of the granular packing. The index is found to have a strong correlation to the cyclic mobility of the granular packing in the post-liquefaction stage. The study provides significant insights into the fundamental mechanisms of cyclic mobility and liquefaction in granular soils from micromechanical perspectives.

Introduction

Understanding the fundamental mechanism of liquefaction in granular soils is one of the major challenges in constitutive modeling of geomaterials. Here, liquefaction refers to a range of phenomena including flow liquefaction and cyclic mobility. Flow liquefaction often occurs in very loose sands, characterized by a sudden loss of the soil strength and is often associated with large deformations and a flow-type failure. On the other hand, cyclic mobility can occur in a much broader range of soils and site conditions than flow liquefaction. It is characterized by progressive accumulation of shear deformations and progressive reduction in effective stress under cyclic loading, and has the potential to result in unacceptably large permanent displacements. Both flow liquefaction and cyclic mobility can cause severe damage to civil structures during earthquakes.

Liquefaction of granular soil has been studied for more many years. Most studies have been focused on determining the triggering of the initial liquefaction and the liquefaction resistance of different soils under various loading conditions. Here, “initial liquefaction” is

[1]Graduate Student, Dept. of Civil and Environmental Engineering, Hong Kong University of Science and Technology, Clear Water Bay, Kowloon, Hong Kong
[2] Corresponding author. Assistant Professor, Dept. of Civil and Environmental Engineering, Hong Kong University of Science and Technology, Clear Water Bay, Kowloon, Hong Kong. Email: gwang@ust.hk

Wei J., Wang G. Cyclic mobility and post-liquefaction behaviors of granular soils under cyclic loading: micromechanical perspectives. *Proceedings of the 10th National Conference in Earthquake Engineering*, Earthquake Engineering Research Institute, Anchorage, AK, 2014.

termed to indicate the first time that the effective stress reaches zero during cyclic undrained loading (Seed and Lee, 1966). Soil behaviors before and after the initial liquefaction can be quite different. Many lab tests had shown that large deformation always occurred after initial liquefaction, i.e., the post-liquefaction stage. In this paper, discrete element simulation is performance to study the micromechanical behaviors of granular soils in the cyclic mobility and post-liquefaction process. The micromechanical study can provide significant insight into a deeper understanding of the fundamental mechanisms of soil behaviors.

Discrete Element Simulation

Discrete element method (DEM) has been a proven tool to effectively simulate the micromechanical behavior of soils during liquefaction (e.g., Ng and Dobry 1994; Sitharam *et al.* 2009). In this study, an open source DEM code, Yade, is used to conduct the numerical simulations. 16,000 poly-dispersed clumped particles are randomly generated in a square representative volume element (RVE). Periodic boundary is prescribed on this RVE to eliminate the non-uniformity caused by RVE boundary. Each clumped particle consists of two partially overlapped disc-shaped particles as shown in Fig. 1. The radius of the particle equals to the radius of a disc-shaped particle having the same area as the clump. If the radius of the disc-shaped particle is r, the radius of the clumped particle R=1.268r. The radius of particles ranges from 0.15mm to 0.45mm and the mean radius R_{50}=0.3mm. A nonlinear Hertz-Mindlin model was used to describe the particle contact behavior. The following material properties are assigned to all the particles: Young's modulus of 70GPa, Possion's ratio of 0.3, friction coefficient of 0.5. Since the simulation is quasi-static, the density of particles is scaled by a factor of 2×10^5 in order to reduce the computational time without affecting the solutions. After particles generation, the packing was isotropically consolidated under an initial confining pressure p=120 kPa to reach a void ratio of 0.228.

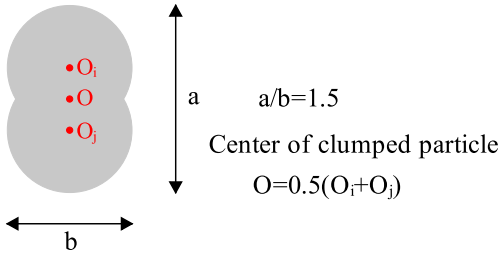

Figure 1. Shape of a clumped particle.

During undrained cyclic simple-shear test, a constant strain rate of 0.01/s was applied in order to ensure the quasi-static condition. The simulation was stress controlled with a cyclic stress ratio (CSR) of 0.2. The pore water pressure is determined by the difference of stress between the vertical total stress and the vertical effective stress. Fig. 2(a) shows the relationship between shear stress (τ) and shear strain (γ). Fig. 2(b) shows the evolution of shear stress (τ) with the effective vertical stress (σ_v). The soil sample reached initial liquefaction after 17 cycles. The simulation result is quantitatively similar to the laboratory test results of a dense granular soil sample. Typical behaviors can be observed from the DEM simulation, such as the gradual decrease of effective vertical stress σ_v in each load cycle till liquefaction, increase of shear strain γ with the number of load cycles, and phase transform from contraction to dilation in each load cycle.

For a granular packing, the effective stress is transmitted through particle contacts. The coordination number is defined as $Z=2N_c/N_p$ (where N_c is the total number of contacts and N_p is the total number of particles). The coordination number is a good indicator of the micromechanical structure of the packing since it represents the average number of contacts for each particle. The coordination number initially progressively decreases from about 4.3 to about 3 with each loading cycle, but then begins a pattern of alternating between incrementally decreasing and incrementally increasing. The cyclic variation in the contact number is qualitatively similar to the cyclic variation in the effective stress, and shows similar butterfly shaped loops in Fig. 2(c) after initial liquefaction is triggered.

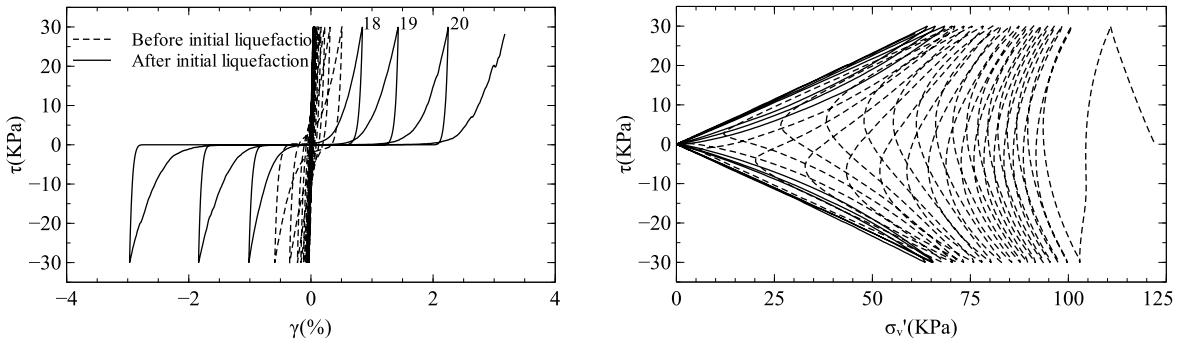

(a) Shear stress and shear strain relation (b) Shear stress and effective vertical stress relation

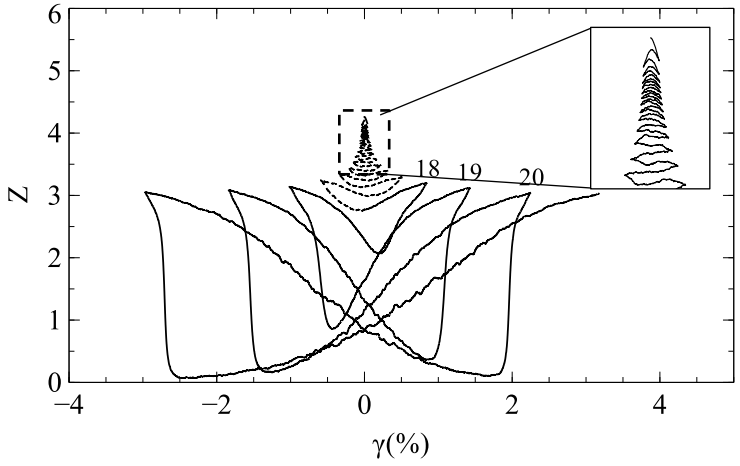

(c) Evolution of coordination number

Figure 2. Macroscopic behavior of granular packing from DEM.

Micromechanical Structure during Cyclic Loading and Post-liquefaction

Evolution of the Contact Number

Under undrained cyclic loading, liquefied sand experiences a flow stage and eventually regains its strength under shear deformation, which is regarded as shear-induced dilatancy, i.e., the tendency of the granular matter to dilate under shear deformation. Fig. 3 shows the evolution of the coordination number versus the shear stress during cycle No. 20. The shear stress remains

almost zero at point 0 and starts to increase when the shear strain γ=0.92% at point 1, where the shear stress reaches 0.1kPa. This stage is denoted as the "flow stage". The "flow stage" was followed by a "hardening stage" when the shear stress starts to grow substantially to 30 kPa and the coordination number reaches 3.04 from point 1 to 2. The number of contacts established at the end of the flow stage (i.e., point 1) is about 75% of the number established at the peak stress point (i.e., point 2). These contacts form a load-carrying structure that permits stress to increase during further shear deformation. Another interesting phenomenon observed from the Fig.3 is that upon unloading from point 2 to 3, the coordination number decreases dramatically to reach a minimum value (Z=0.1), implying that the load-carrying structure is completely destroyed upon unloading.

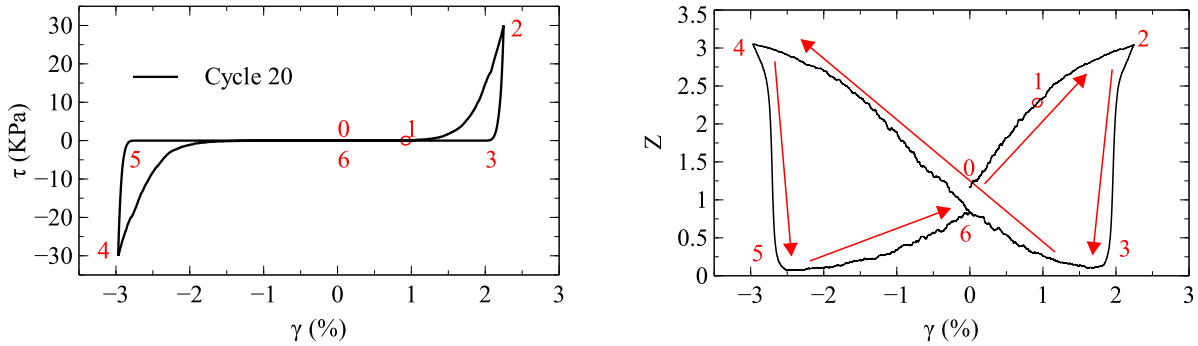

(a) Shear stress and shear strain relation (b) Evolution of coordination number

Figure 3. Shear stress and coordination number evolution during cycle 20

Fig. 4 shows the relation between coordination number Z and shear stress in all loading cycles. It is observed that a minimum coordination number (Z=2.28) is required for stress hardening in each cycle. The threshold Z value can thus be defined as the microscopic criterion for stress hardening in the post-liquefaction stage. When Z is below the threshold, the packing is under the flow liquefaction state and the load-carrying structure cannot be fully formed.

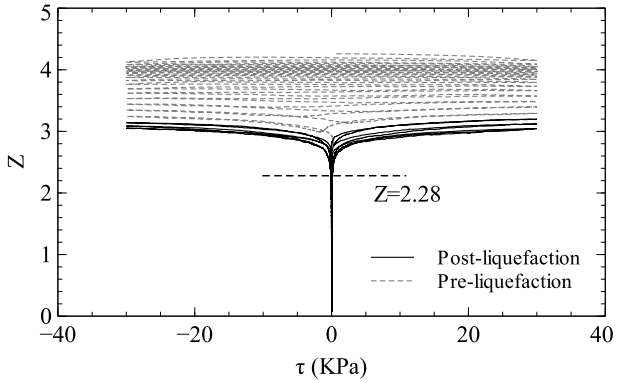

Figure 4. Relation between coordination number and shear stress

Local strain measurement

Although the coordination number is a good indicator to quantify the overall structure of

granular packing, it cannot explain how such a structure is formed. To answer this question, we measure the local strain change during the shear deformation to investigate the change of local structure. In the 2D DEM simulation, we use Delaunay tessellation to divide the granular packing into triangle elements. The local strain is calculated using these triangle elements. For triangular element *i*, the local strain tensor $\varepsilon_{\alpha\beta}^{(i)}$ can be calculated from the position and displacement vectors of the element's nodal particles:

$$\varepsilon_{\alpha\beta}^{(i)} = \frac{1}{2}\left(\bar{e}_{\alpha\beta}^{(i)} + \bar{e}_{\beta\alpha}^{(i)}\right) \tag{1}$$

$$\bar{e}_{\alpha\beta}^{(i)} = \frac{1}{S^{(i)}}\int_{S^{(i)}} e_{\alpha\beta}^{(i)} ds = \frac{1}{S^{(i)}}\int_{S^{(i)}} \frac{\partial u_{\alpha}^{(i)}}{\partial x_{\beta}^{(i)}} ds = \frac{1}{S^{(i)}}\oint_{\partial S^{(i)}} u_{\alpha}^{(i)} n_{\beta}^{(i)} dl \tag{2}$$

One can refer to Bagi (1996) for detailed information of the above formulation. Accordingly, the deviatoric local strain $\varepsilon_q^{(i)}$ for element *i* can be defined in Eq. (3).

$$\varepsilon_q^{(i)} = \sqrt{\frac{2}{3}\left(\varepsilon_{\alpha\beta}^{(i)} - \frac{1}{3}\delta_{\alpha\beta}\varepsilon_{kk}^{(i)}\right)\left(\varepsilon_{\beta\alpha}^{(i)} - \frac{1}{3}\delta_{\alpha\beta}\varepsilon_{kk}^{(i)}\right)} \tag{3}$$

In order to have a better comparison, the deviatoric local strain is normalized by the averaged deviatoric local strain in the packing:

$$\bar{\varepsilon}_q^{(i)} = \frac{\varepsilon_q^{(i)}}{\sum_i^N \varepsilon_q^{(i)} / N} \tag{4}$$

During the loading cycle number 20, the shear strain increases from 0% to 2.25%. Correspondingly, the packing evolves from a flow stage at the initial point γ=0% to reach a shear stress of 30 kPa at the end point γ=2.25%. To investigate the change in local strain measures, the shear strain is divided into five intervals with a strain increment $\Delta\gamma$=0.45% as shown in Fig. 5. The first two intervals belong to the flow stage and the last two intervals below to the hardening stage. The 3th interval is a transition stage when the stress just starts to grow. The displacement of each particle in the local strain calculation is based on particle position difference during the current strain increment. Fig. 6 shows the contour of normalized deviatoric local strain increment for each strain increment. During the first strain increment $\Delta\gamma_1$, the distribution of strain increment is quite uniform. Similar pattern is also observed in the second strain increment $\Delta\gamma_2$. However start from the third strain increment, large change in the local strain begins to concentrate in some positions, implying that particle adjustment gradually becomes localized. This kind of pattern is also shown in the following strain increments.

In the discussion about the evolution of the coordination number, we mentioned that the load-carrying structure is primarily formed during the "flow stage". From the emergence of strain localization, we can deduce the morphology of the load-carrying structure: during the beginning of the flow stage, particles are dispersed with few local contacts. Adjustment of particle is not restricted and change in local strain during this stage is uniformly distributed. However continuing shear deformation will organize some particles to form bigger clusters.

Relative displacement between particles in the cluster is restricted. Adjustment of relative positions mainly occurs between these clusters. That can explain why local strains will be gradually localized.

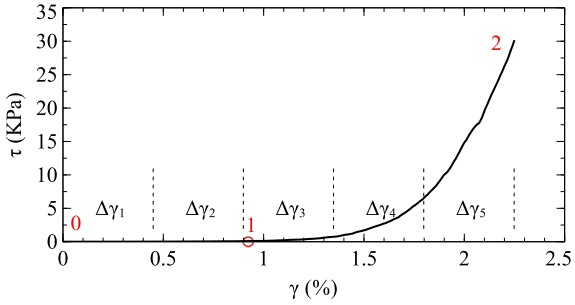

Figure 5. Five strain increments

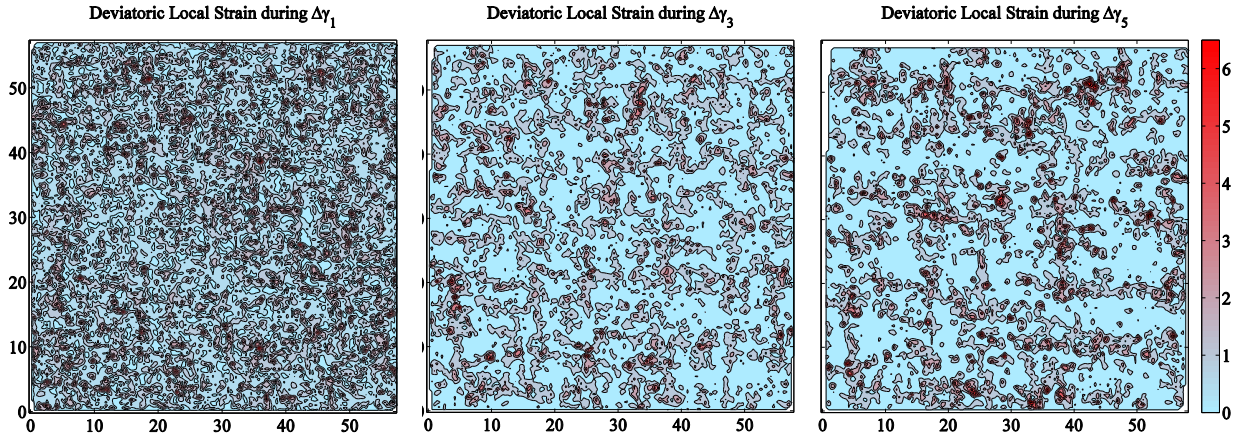

Figure 6. Contours of normalized deviatoric local strain increment $\Delta\bar{\varepsilon}_q^{(i)}$ in each strain increment.

Evolution of the non-affine displacement field

The micromechanical structure can also be further demonstrated using non-affine displacement (Goldenberg *et al.* 2007). The non-affine displacement is calculated by subtracting the affine displacement from the total displacement. Denoting the center position vector of particle *i* as $\mathbf{x}_n^{(i)}$ if the global strain is $\boldsymbol{\varepsilon}_n$, and $\mathbf{x}_{n+1}^{(i)}$ when the global strain is $\boldsymbol{\varepsilon}_{n+1}$, the displacement increment of particle *i* is $\Delta\mathbf{u}_{n+1}^{(i)} = \mathbf{x}_{n+1}^{(i)} - \mathbf{x}_n^{(i)}$. The affine displacement of particle *i* is defined as $\Delta\boldsymbol{\varepsilon}_{n+1} \cdot \mathbf{x}_n^{(i)}$, where $\Delta\boldsymbol{\varepsilon}_{n+1}$ is the global strain increment ($\Delta\boldsymbol{\varepsilon}_{n+1} = \boldsymbol{\varepsilon}_{n+1} - \boldsymbol{\varepsilon}_n$). The non-affine particle displacement for particle *i* is defined as:

$$\delta\mathbf{u}_{n+1}^{(i)} = \Delta\mathbf{u}_{n+1}^{(i)} - \Delta\boldsymbol{\varepsilon}_{n+1} \cdot \mathbf{x}_n^{(i)} \tag{5}$$

Fig. 7 shows the non-affine displacement field for the first and the last strain increment. For a better comparison, the non-affine displacement field is normalized by its mean value:

$$\overline{\delta \mathbf{u}_{n+1}^{(i)}} = \frac{\delta \mathbf{u}_{n+1}^{(i)}}{\sum_i^N \delta \mathbf{u}_{n+1}^{(i)} / N} \tag{6}$$

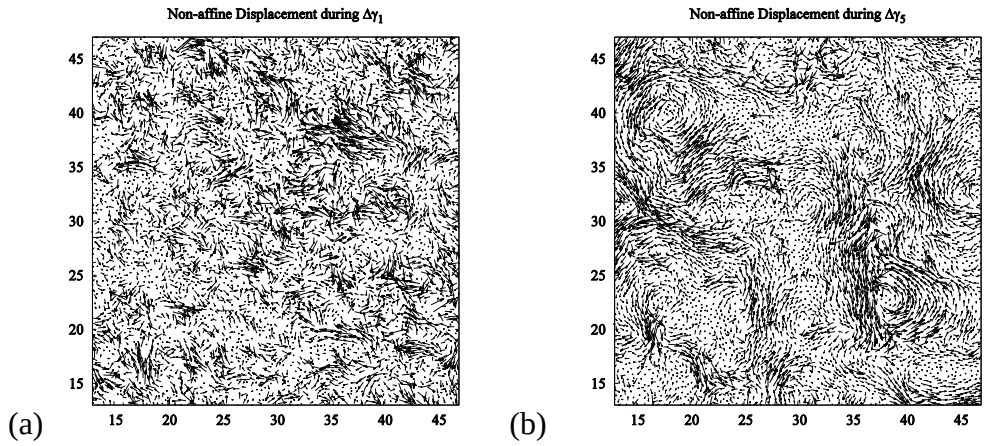

(a) (b)

Figure 7. Non-affine displacement field of the first and the last strain increment

It can be observed that the non-affine displacement field is quite random during the first strain increment (Fig. 7(a)), which implies that the particle movement is not significantly constrained from its surrounding particles. However, in the last strain increment, many distinctive 'flow bands' and 'vortex' can be observed. Particles within the 'flow bands' will normally have similar velocity with its surrounding particles. In order to characterize the non-affine displacement field, a spatial correlation function *C* is used. The function *C* is defined as:

$$C(R) = \frac{\sum_{i,j}\left[\rho\left(\delta\mathbf{u}^{(i)}, \delta\mathbf{u}^{(j)}\right)\phi\left(\left|D_{ij} - R\right|\right)\right]}{\sum_{i,j}\phi\left(\left|D_{ij} - R\right|\right)} \tag{7}$$

$$\rho\left(\delta\mathbf{u}^{(i)}, \delta\mathbf{u}^{(j)}\right) = \frac{2\delta\mathbf{u}^{(i)} \cdot \delta\mathbf{u}^{(j)}}{\left|\delta\mathbf{u}^{(i)}\right|^2 + \left|\delta\mathbf{u}^{(j)}\right|^2} \tag{8}$$

$$\phi\left(\left|D_{ij} - R\right|\right) = \begin{cases} 1 & \left|D_{ij} - R\right| < 0.5\left(r^{(i)} + r^{(j)}\right) \\ 0 & \left|D_{ij} - R\right| \geq 0.5\left(r^{(i)} + r^{(j)}\right) \end{cases} \tag{9}$$

where $D_{ij} = \left|\mathbf{x}^{(i)} - \mathbf{x}^{(j)}\right|$ is the center-to-center distance between particle *i* and *j*, $r^{(i)}$ and $r^{(j)}$ are the radius of particle *i* and *j*. $\rho\left(\delta\mathbf{u}^{(i)}, \delta\mathbf{u}^{(j)}\right)$ is the correlation between two vectors. $\rho\left(\delta\mathbf{u}^{(i)}, \delta\mathbf{u}^{(j)}\right)$ =1 only if $\delta\mathbf{u}^{(i)} = \delta\mathbf{u}^{(j)}$. If $\delta\mathbf{u}^{(i)}$ is normal to $\delta\mathbf{u}^{(j)}$, $\rho\left(\delta\mathbf{u}^{(i)}, \delta\mathbf{u}^{(j)}\right)$ =0. The minimum correlation -1 is achieved only if $\delta\mathbf{u}^{(i)} = -\delta\mathbf{u}^{(j)}$. $\phi\left(\left|D_{ij} - R\right|\right)$ specifies a bin to include particle pairs $\left\{\mathbf{x}^{(i)}, \mathbf{x}^{(j)}\right\}$ for a given *R* value. Particle pairs are counted into *C*(*R*) calculation only

if $R-0.5\left(r^{(i)}+r^{(j)}\right)<D_{ij}<R+0.5\left(r^{(i)}+r^{(j)}\right)$. Fig. 8 shows the spatial correlation $C(R)$ of the non-affine displacement increases from the flow stage to the hardening stage.

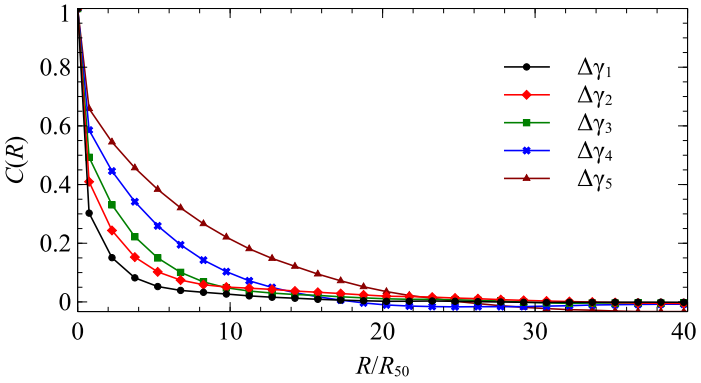

Figure 8. Spatial correlation during each stage

Evolution of Microscopic Configuration in Post-Liquefaction

Definition of Centroid Distance (D_c)

For 2D simulation, Voronoi cell can be conveniently used to divide the void space around each particle. As shown in Fig. 9, the Voronoi cell for particle *i* is a convex polygon enclosed by C_1-C_2-C_3-C_4-C_5. The mass center of the Voronoi cell and the mass center of the particle are denoted as O^i and P^i, respectively. The centroid distance D_c for particle *i* can be defined as:

$$D_c^i = \frac{\left|P^i - O^i\right|}{R_{50}} \tag{10}$$

where R_{50} is the average radius of particles.

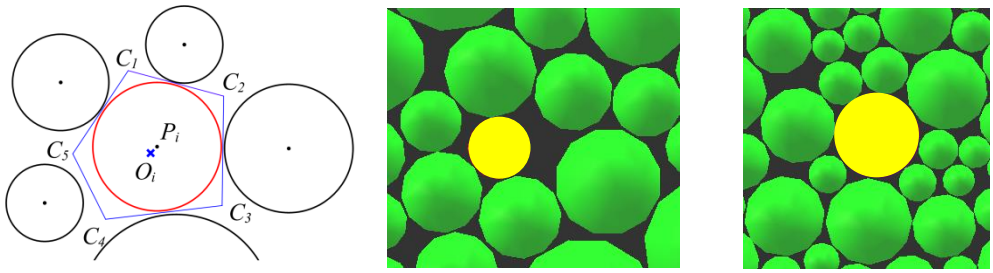

(a) Voronoi cell (b) large D_c^i (c) small D_c^i

Figure 9. Definition of D_c

Accordingly, the centroid distance (D_c) of the whole packing can be defined as the average of D_c^i for all particles:

$$D_c = \frac{1}{N}\sum_i^N D_c^i \tag{11}$$

where N is the number of particles. Fig. 8(a) and Fig. 8(b) illustrate two typical cases to demonstrate the physical meaning of D_c. From this figure, the particle with a large D_c^i is surrounded by a larger void space, which means a loose local configuration. The particle with a small D_c^i is more likely to be located in a dense configuration. It is worth pointing out that an individual particle within a loose local configuration may also attain a small D_c^i. However, the probability of such a case is rather low. This observation demonstrates that D_c^i can be used to represent the local configuration of the packing.

Two undrained cyclic simple tests are conducted under strain-controlled condition, where the prescribed shear strain is constant (3% and 4.5%) during each cycle. In the DEM simulation, disk-shaped particles are used for convenience of calculating D_c. Fig. 10 shows evolution of D_c value evaluated at the zero strain in each loading cycle. The D_c decreases during the first several cycles and oscillate around a constant value after 50 loading cycles. The influence of the prescribed strain level to the evolution of D_c can also be observed in Fig. 10. The strain levels only affect the decreasing rate of D_c but do not affect the asymptotic value of D_c. Snapshots of particle configurations before the first and during the 100th loading cycle are demonstrated in Fig. 11. In these figures, red color is used to highlight particles whose D_c^i value decreases between two configurations, while green color highlights particles with a decreased D_c^i. The majority of particles are in gray color, whose D_c^i values are almost unchanged during cyclic loading. Consistent with the observation that the global D_c is decreasing, the number of red particles is significant greater than the green particles. Relative large pores are found surrounding the red particles in the initial configuration (marked by circles). However, these large pore space diminishes in the final configuration. So the effect of undrained cyclic loading is to redistribute these relative large pores. On the other hand, large pores are occupied by particles and are reduced by densification of granular packing under a drained cyclic loading.

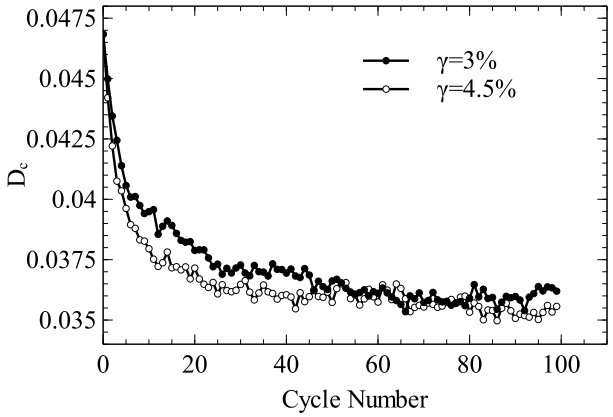

Figure 10. Evolution of D_c with different strain level

The presence of relative large pores can be regarded as source of inhomogeneity for the granular packing. Due to the friction between granular particles and complex particle shape,

local arching can be formed during the phase of initial consolidation. The local arching preserves relative large pores. Under the same stress condition, more relative large pores can be observed in the loose pacing compared with the dense or medium packing. However, the arching structure is not stable and can be easily destroyed by the cyclic loading. Large pores are redistributed and the packing is more homogeneous as a result. The decreasing trend of D_c implies that the effect of cyclic loading progressively transforms the packing into a more homogenous configuration.

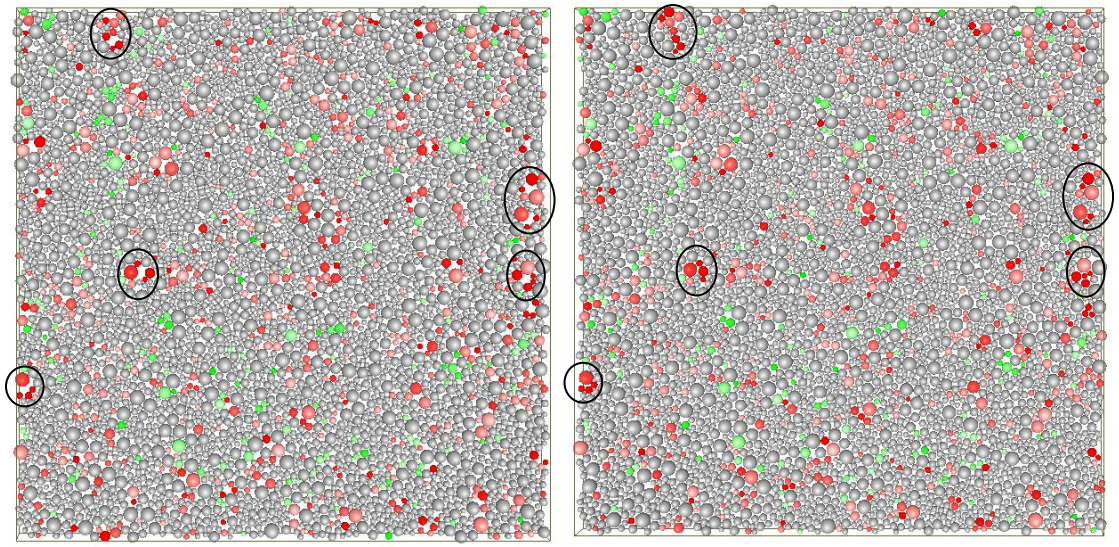

(a) Before cyclic loading (b) Cycle number 100

Figure 11. Change of packing configuration

Evolution of D_c and Cyclic Mobility in Post-liquefaction Stage

In a load-controled cyclic simple shear test, the maximum strain developed in the soil continues to accumulate with increasing number of cycles (cf. Fig. 1(a)). Through the DEM simulation, we observed that the cyclic mobility of the granular packing is strongly corrected to the evolution of D_c. Here, we use γ_c to measure the mobilized maximum strain in each load cycle. For example, γ_c is calculated as the shear strain between point 2 and 4 in Fig. 3(a) for load cycle No. 20. However, the continued increase of γ_c with increasing load cycles can only be observed in dense or medium dense packing under a limited number loading cycles. It is interesting to ask: whether γ_c can reach an ultimate value and will no longer increase with further loading cycles?

Fig. 12(a) shows the DEM simulation result of shear stress τ and shear strain γ behaviors under 60 loading cycles. The evolution of γ_c and D_c with the number of cycles are shown in Fig. 12(b). Similar to the previous strain-controlled case, D_c decreases with increasing number of cycles and it reaches a lower limit after 30 cycles. Interestingly, when D_c reaches its lower limit, the mobilized maximum shear strain γ_c also stabilizes around a constant value. The maximum shear strain ceases to increase under further loading cycles, and the stress-strain behavior of the soil is saturated. It implies that the mobilized maximum shear strain is closely related to the packing configuration. The ultimate stage of cyclic mobility exists and it can be reached.

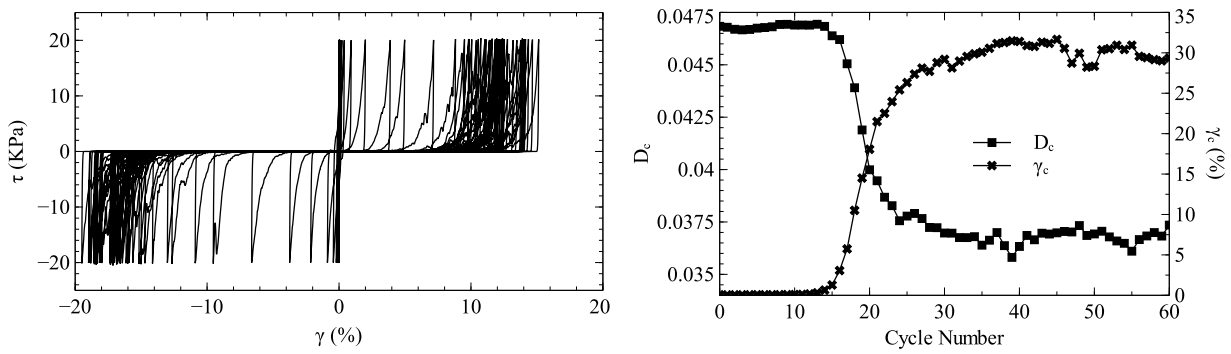

Figure 12. Simulation result of stress-control test with CSR=0.2: (a) stress-strain relation (b) evolution of γ_c and D_c with the number of cycles

Conclusions

In this paper, the micromechanical behavior of granular materials during the cyclic loading and post-liquefaction stage is investigated using DEM. The post-liquefaction stress-strain behavior is characterized by an initial flow stage, followed by stress hardening. In the flow stage, although the effective stress is almost zero, a load-carrying is gradually formed. However, the load carrying structure can be easily destroyed by unloading. During the formation of such load-carrying structure, particle deformation tends to localize. Relative position adjustment will be concentrated between bigger clusters of particles. Furthermore, an index for the packing configuration is defined using centroid distance D_c. During cyclic loading, it is observed that D_c will decrease and eventually reaches around a lower limit. Through the DEM simulation, we observed that the cyclic mobility of the granular packing in the post-liquefaction is strongly corrected to the evolution of D_c. When D_c reaches to the final value, the cyclic mobility in the granular packing also reaches to its ultimate state. The maximum shear strain will stop to accumulate with further cyclic loading. Finally, it should be noted that all presented results are based on 2D DEM simulations. One may expect similar behaviors in a true 3D system, and it will be the subject of our future study.

Acknowledgements

The study was financially supported by RGC grant 620311and DAG11EG03G.

References

1. Seed HB, Lee KL. Liquefaction of saturated sands during cyclic loading, *J. Soil Mech. Found. Div.* 1966; **92**:105-134.
2. Ng TT, Dobry R, Numerical simulations of monotonic and cyclic loading of granular soil. *Journal of Geotechnical Engineering* 1994; **120** (2):388-403.
3. Bagi K. Stress and strain in granular assemblies. *Mechanics of Materials* 1996; **22** (3), 165-177.
4. Sitharam TG, Vinod JS, Ravishankar BV. Post-liquefaction undrained monotonic behavior of sands: experiments and DEM simulations, *Géotechnique* 2009; **50**(1):43-53
5. Goldenberg C, Tanguy A, Barrat JL. Particle displacements in the elastic deformation of amorphous materials: local fluctuations vs. non-affine field, *Europhysics Letters* 2007; **80**:16003.